







# Centennial scale sequences of environmental deterioration preceded the end-Permian mass extinction

Received: 30 July 2022

Accepted: 28 March 2023

Published online: 14 April 2023

 Check for updates

Ryosuke Saito <sup>1,2,3,4</sup> ✉, Lars Wörmer <sup>1</sup>, Heidi Taubner <sup>1</sup>, Kunio Kaiho <sup>5</sup>, Satoshi Takahashi<sup>6</sup>, Li Tian <sup>7</sup>, Masayuki Ikeda<sup>8</sup>, Roger E. Summons <sup>2</sup> & Kai-Uwe Hinrichs<sup>1</sup>

The exact drivers for the end-Permian mass extinction (EPME) remain controversial. Here we focus on a ~10,000 yr record from the marine type section at Meishan, China, preceding and covering the onset of the EPME. Analyses of polyaromatic hydrocarbons at sampling intervals representing 1.5–6.3 yr reveal recurrent pulses of wildfires in the terrestrial realm. Massive input pulses of soil-derived organic matter and clastic materials into the oceans are indicated by patterns of C<sub>2</sub>-dibenzofuran, C<sub>30</sub> hopane and aluminum. Importantly, in the ~2,000 years preceding the main phase of the EPME, we observe a clearly defined sequence of wildfires, soil weathering, and euxinia provoked by the fertilization of the marine environment with soil-derived nutrients. Euxinia is indicated by sulfur and iron concentrations. Our study suggests that, in South China, centennial scale processes led to a collapse of the terrestrial ecosystem ~300 yr (120–480 yr; ± 2 s.d.) before the onset of the EPME and that this collapse induced euxinic conditions in the ocean, ultimately resulting in the demise of marine ecosystems.

The end-Permian mass extinction (EPME) was the most severe of the Phanerozoic, impacting both the marine and terrestrial biospheres with ~90% marine species loss and ~70% land-based vertebrate family loss<sup>1</sup>. The favored hypothesis is that contemporaneous emplacement of the Siberian Traps Large Igneous Province (LIP) was the primary driver<sup>2,3</sup>. The Siberian Traps eruptions could have induced a chain of deleterious environmental impacts, including shallow marine anoxia<sup>4</sup>, lethal temperatures<sup>5</sup>, emission of toxic metals<sup>6</sup>, emission of climate-modifying volcanic gases (e.g., SO<sub>2</sub> and CO<sub>2</sub>), wildfires, destruction of atmospheric ozone, acid rain, and the promotion of weathering of fresh volcanic rocks<sup>1</sup>.

As Siberian Traps eruptions have a reported duration of at least 900 kyr<sup>3,7</sup>, it remains to be explained what triggered the 60 ± 48 kyr marine mass extinction event<sup>8,9</sup> within the Permian-Triassic transitional interval<sup>10,11</sup>. Heterogeneity of Siberian Traps activity concerning the magnitude of eruptions and emplacement style (e.g., intrusive vs. eruptive) has been introduced as a potential explanation for high-intensity events at decadal to centennial time scales<sup>3,10,11</sup>. Given the difficulty in elucidating a decadal- to centennial-scale volcanic history from the volcanic rock relics in Siberia, various direct or indirect chemical tracers (e.g., Hg) have been introduced to track LIP activity<sup>12–15</sup>. Some of these studies suggest that the strong volcanic

<sup>1</sup>MARUM - Center for Marine Environmental Sciences & Faculty of Geosciences, University of Bremen, 28359 Bremen, Germany. <sup>2</sup>Department of Earth, Atmospheric and Planetary Sciences, Massachusetts Institute of Technology, 45 Carleton Street, Cambridge, MA 02142, USA. <sup>3</sup>Graduate School of Sciences and Technology for Innovation, Yamaguchi University, 1677-1 Yoshida, Yamaguchi City 753-8512, Japan. <sup>4</sup>Japan Science and Technology Agency, PRESTO, 4-1-8 Honcho, Kawaguchi, Saitama 332-0012, Japan. <sup>5</sup>Department of Earth Science, Tohoku University, Sendai 980-8578, Japan. <sup>6</sup>Department of Earth and Environmental Sciences, Graduate School of Environmental Studies, Nagoya University, Nagoya 464-8601, Japan. <sup>7</sup>The Key Laboratory of Biogeology and Environmental Geology and Faculty of Earth Science, China University of Geosciences Wuhan, Wuhan 430074, China. <sup>8</sup>Department of Earth and Planetary Science, University of Tokyo, Bunkyo 113-0033, Japan. ✉e-mail: [olivinline@yahoo.co.jp](mailto:olivinline@yahoo.co.jp)

activity at the end-Permian was pulsatile<sup>16</sup>, and that for both marine and terrestrial extinctions to occur, the destruction of terrestrial ecosystems had to take place first<sup>17–19</sup>. Global climate simulations of flood basalt gas emissions, described by sulfur chemistry and aerosol microphysics coupled with atmosphere-ocean circulation, predict perturbations on scales of several hundred years<sup>11</sup>. Detailed, high-resolution (mm-scale or higher) investigations of tracers for volcanic activity, terrestrial ecosystem collapse, and marine environmental degradation are thus needed to clarify the sequence of these events and their causal relation to the biotic extinction.

Among the suite of sedimentary molecular biomarkers, polycyclic aromatic hydrocarbons (PAHs) have been proposed to track combustion events such as wildfires, volcanic activity, and asteroid impacts<sup>20–22</sup>. Additionally, C<sub>2</sub>-dibenzofuran (C<sub>2</sub>-DBF), a compound of predominantly terrestrial origin, has been detected in sediments<sup>17</sup>. Furans are produced by the dehydration of polysaccharides such as cellulose, which are typically abundant in litter and soils<sup>23</sup>. Thus, PAHs and C<sub>2</sub>-DBF have previously been used, at cm-resolution or coarser, as a marker of the devastation of terrestrial ecosystems at the EPME<sup>17,21,24</sup>.

The method of mass spectrometry imaging (MSI) was recently implemented for geoscientific applications to extract climate records from marine sediments at ultra-high temporal resolution<sup>25,26</sup>. We here conduct an MSI analysis of molecular biomarkers at 0.1 mm resolution on the uppermost Permian of the Changhsing Formation in the marine Meishan section, i.e., the Global Stratotype Section and Point (GSSP) for the Permian-Triassic boundary<sup>27</sup>. During the late Permian, the Meishan region in South China was located in the low-latitude eastern Paleotethys Ocean (Fig. 1). According to conodont age-diagnostic fossil zones, the Meishan section covers the upper Permian to Lower Triassic, including the EPME<sup>28,29</sup>, archiving data of terrestrial and marine origin. We pair MSI analysis with records of elemental composition at 0.05-mm resolution obtained by micro-X-ray fluorescence spectroscopy (micro-XRF) to provide insight into the contribution of clastic material and provenance as well as redox conditions<sup>30,31</sup>. Moreover, in order to validate the robustness of MSI analysis, conventional molecular biomarker analysis by gas chromatography-mass spectrometry (GC-MS) is conducted at 1–5 cm-resolution. Our combined biomarker and elemental data thus reveal the fine-scale pattern of environmental change in the terrestrial and oceanic realms leading to the EPME recorded in the near-shore marine succession at Meishan.

## Results and discussion

### Fire events on a multi-century scale

Strong variability in the intensity of combustion events is identified in the ~10,000 yr succession leading to the EPME<sup>32</sup>, based on the PAH data. Four millennial-scale intervals of increased PAH accumulation are

identified through GC- and MSI-based analyses (intervals A–D in Fig. 2 and Supplementary Fig. 1). The agreement between both techniques confirms the robustness of the obtained data. A sub-decadal resolution offered by MSI further reveals the pulsed nature of the PAH signal. Eight major combustion episodes are clearly distinguishable (events 1–8 in Fig. 2 and Supplementary Fig. 2) coupled with numerous smaller peaks. We estimate the mean duration of these events to be  $270 \pm 150$  yr (mean  $\pm$  s.d.) (Supplementary Table 1). Their intensity and frequency increased towards the top of the analyzed section, an observation that is also supported by wavelet analysis (Supplementary Fig. 3).

Records of C<sub>2</sub>-DBF and PAHs are positively correlated (Figs. 2, 3). We interpret this as the result of wildfires that removed the vegetative cover (See Supplementary Discussion), thus leaving soils exposed to enhanced weathering and erosion, as observed in modern environments and discussed for the EPME<sup>33</sup>. Simultaneously, this correlation suggests that PAHs were mainly transported to the marine environment through surface runoff, along with abundant soil-derived organic matter. From interval B upwards, elevated aluminum abundances coincide with peaks of PAHs. Accumulation of Al in the marine record could be indicative of weathering, and/or Al leaching from soils due to acid rain<sup>1,34</sup>.

The ratio between different PAH species can provide insight into the formation conditions of the PAHs detected in sedimentary rocks. Larger molecules of PAHs (e.g., the seven-ringed coronene) require a higher temperature to form due to kinetic limitations to the successive addition of rings<sup>35</sup>. Consequently, the geological record of past volcanogenic combustion<sup>20</sup> and asteroid impacts<sup>22</sup> show a higher relative abundance of larger ringed PAHs, especially coronene. At the end-Permian, injections to the stratosphere from Siberian Traps volcanism resulted in a widespread distribution of relatively enhanced coronene concentrations and a positive correlation with mercury (Hg)<sup>21</sup>. By contrast, in modern wildfire PAH records, seven-ringed PAH are less abundant due to the relatively low combustion temperature<sup>36</sup>. We use the ratio of seven-ringed vs five-ringed PAHs (PAH<sup>7/5</sup>)<sup>20</sup> as a proxy for investigating the intensity of combustion events in the GSSP Meishan record.

The PAH<sup>7/5</sup> values remain relatively low across the entire sampled record, with the exception of the ~3000 yr period between intervals A and B, where the lowest concentrations of PAH and C<sub>2</sub>-DBF, but the highest values of PAH<sup>7/5</sup>, are observed (Supplementary Fig. 1). The association of low PAH<sup>7/5</sup> values with highest values of the soil marker C<sub>2</sub>-DBF suggests that soil-derived PAHs are dominated by compounds with smaller numbers of rings (Fig. 3). Accordingly, the high values of PAH<sup>7/5</sup> between intervals A and B (Supplementary Fig. 1) most likely result from the strongly reduced contribution of soil organic matter.



**Fig. 1 | Late Permian global paleogeography.** The Meishan section and Siberian Traps are indicated by yellow star and red area, respectively. source map © 2020 Colorado Plateau Geosystems Inc.

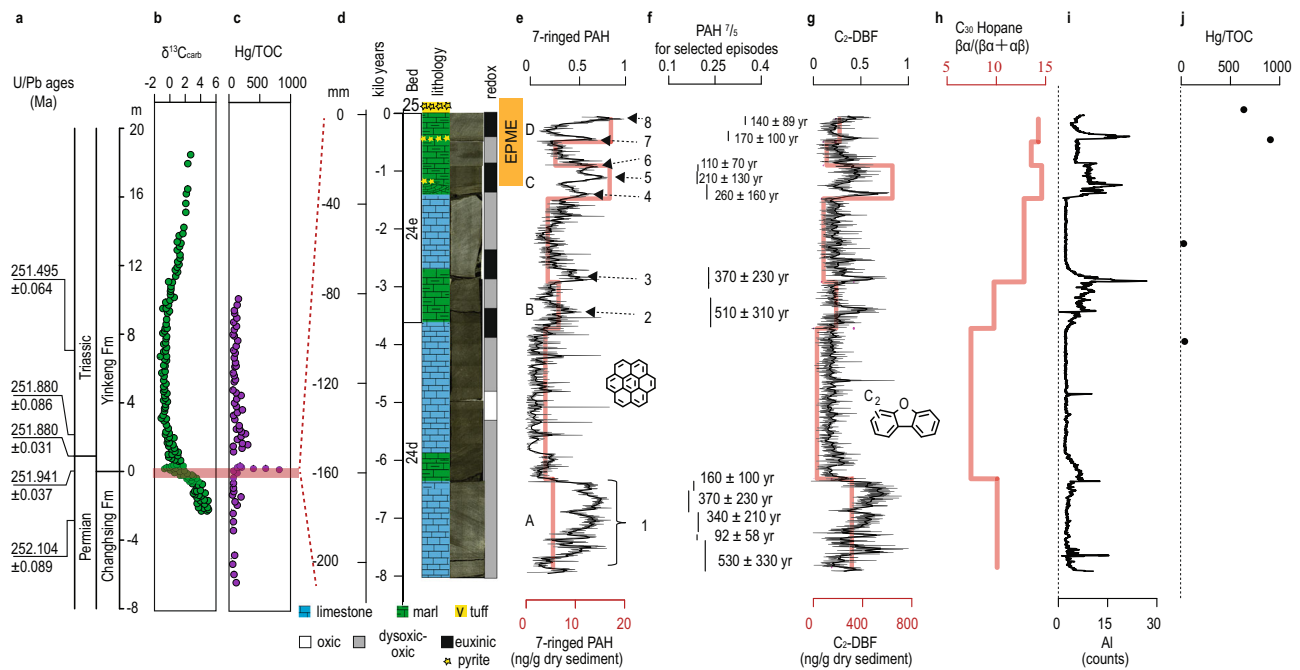


**Fig. 2 | Abrupt environmental deterioration leading to the end-Permian mass extinction: chemostratigraphy of molecular biomarkers and aluminum abundances from the Meishan section, South China.** **a–c** A stratigraphic record (–8 to 20 m) of U/Pb ages<sup>5</sup> (**a**), stable carbon isotopic composition of carbonate<sup>18</sup> (**b**) as a gauge of the carbon cycle and Hg/TOC ratios<sup>18</sup> (**c**) representing volcanogenic Hg concentrated in terrestrial ecosystems. **d–j** An expanded stratigraphic record of the top 200 mm below the base of Bed 25 (0 m) for the lithological column with ages and redox conditions based on framboidal pyrite data<sup>39</sup> (**d**), 7-ringed PAH (**e**) as a combustion marker, PAH<sup>7/5</sup> (**f**) as a combustion temperature marker, C<sub>2</sub>-DBF (**g**) and C<sub>30</sub> hopane βα/(βα + αβ) (**h**) as markers for soil input, aluminum (relative abundance) (**i**) as a marker for clastic input, and the Hg/TOC ratio (**j**). In **d**, the linear

high-resolution age model was constructed using a mean-weighted sedimentation rate (2.6 cm/kyr)<sup>8</sup> (see text). EPME is after ref. 21. In **e**, letters A–D identify intervals of increased PAH concentrations based on the GC analysis, while numbers 1–8 identify single events of increased PAH input based on the MSI analysis. In **f**, solid vertical lines indicate mean values of PAH<sup>7/5</sup> for each of the eight events, while numbers along the lines indicate the inferred duration of each event (mean ± 2 s.d.). In **e**, **g**, **h**, the vertical red lines on each plot are the corresponding depth range of GC-MS data for each sample, black lines show MSI-based data with 0.1 mm resolution. In **e** and **g**, seven-ringed PAH and C<sub>2</sub>-DBF for MSI-based data are normalized to their maximum values; solid black lines are derived from locally weighted scatterplot smoothing (lowess) of the data.

Additionally, very low PAH concentrations in this interval, close or below the detection limit, might result in larger analytical uncertainties and potential mathematical artifacts. Therefore, the evaluation of PAH<sup>7/5</sup> is more informative for events 1–8, which are characterized by high concentrations of biomarkers of both combustion and soil organic matter input; consequently, our interpretation of this ratio focuses on its mean values for these eight events (Figs. 2, 4).

Based on the above-mentioned relationships between C<sub>2</sub>-DBF and PAHs, the increase in PAH<sup>7/5</sup> towards the EPME, and especially in events 7 and 8, tentatively indicates an increase in the proportion of volcanogenic PAHs relative to soil/wildfire-derived PAHs. Higher PAH<sup>7/5</sup> values at the top of the sequence also correspond to the increased Hg/TOC as a result of the accumulation of Hg released globally by volcanic activity (mercury enrichment interval 4)<sup>14</sup> on land, which was transported to the ocean upon the collapse of terrestrial ecosystems<sup>13,18</sup>. While volcanism might have become more intense towards the end of the sequence, we argue that the increase in PAH<sup>7/5</sup>, as well as low abundances of C<sub>2</sub>-DBF and prominent peaks in Al, might also be indicative of the collapse and exhaustion of the terrestrial ecosystems in response to a combination of stressors, such as acid rain, heat, drought, and wildfires<sup>1</sup>.

### Centennial-scale sequence of environmental deterioration

To further evaluate this hypothesis, we concentrate on the uppermost 4 cm (ca. 2000 yr) of our record, which includes the onset of the EPME as defined by the extinction of Paleozoic corals and fusulinids<sup>32</sup>. Statistical analysis based on eighteen fossiliferous sections in south China and peri-Gondwana (Tibet, Kashmir, and the Salt Range of Pakistan) indicates that the EPME starts from the top of Bed 24e with the main

phase being Bed 25 at the GSSP Meishan section<sup>37</sup>. Geochronological and paleontological studies of the Penglaitan section, which is stratigraphically expanded compared to the GSSP Meishan section, further support the main phase of extinction being located at Bed 25<sup>38</sup>. In addition to the molecular and elemental markers described before, we include sulfur (S) abundance (also compared to iron (Fe) to identify pyrite layers) as well as existing framboidal pyrite data<sup>39</sup> as indicators for euxinic conditions in the water column and/or the depositional environment<sup>40</sup> (Fig. 4).

Event 4 at Bed 24e, which immediately preceded the onset of the EPME is characterized by the largest peak of soil organic matter input as indicated by C<sub>2</sub>-DBF; this pulse of soil organic matter input was probably associated with episodes of mass wasting concurrent with, and promoted by, wildfires. Notably, this event is distinguished by the highest values of βα/(βα + αβ) ratios for C<sub>30</sub> hopane isomers, indicative of oxic-soil organic matter input<sup>41</sup>. The occurrence of this event is in line with the terrestrial ecosystem oxidation event, as envisaged by the Hg isotopes and modeling of Hg cycling<sup>18</sup> (Fig. 2). This peak in soil organic matter is followed by a peak in clastic material, indicating that after the topsoil had been stripped, the exposed bedrock may have become more susceptible to weathering and transport to the ocean. The intensity of the C<sub>2</sub>-DBF signal becomes weaker towards event 8 at the top of Bed 24e, following the maximum during event 4, while PAH intensity peaks are about equal during events 4–8 (Fig. 4). After event 4, soil organic matter input thus becomes less prominent. During event 7, a smaller C<sub>2</sub>-DBF maximum coincides with the maximum in Al, indicating that the weathering of soil and bedrock occurred almost simultaneously, probably due to the reduced thickness of the soil soon after the major mass wasting associated with event 4. Event 4 is thus

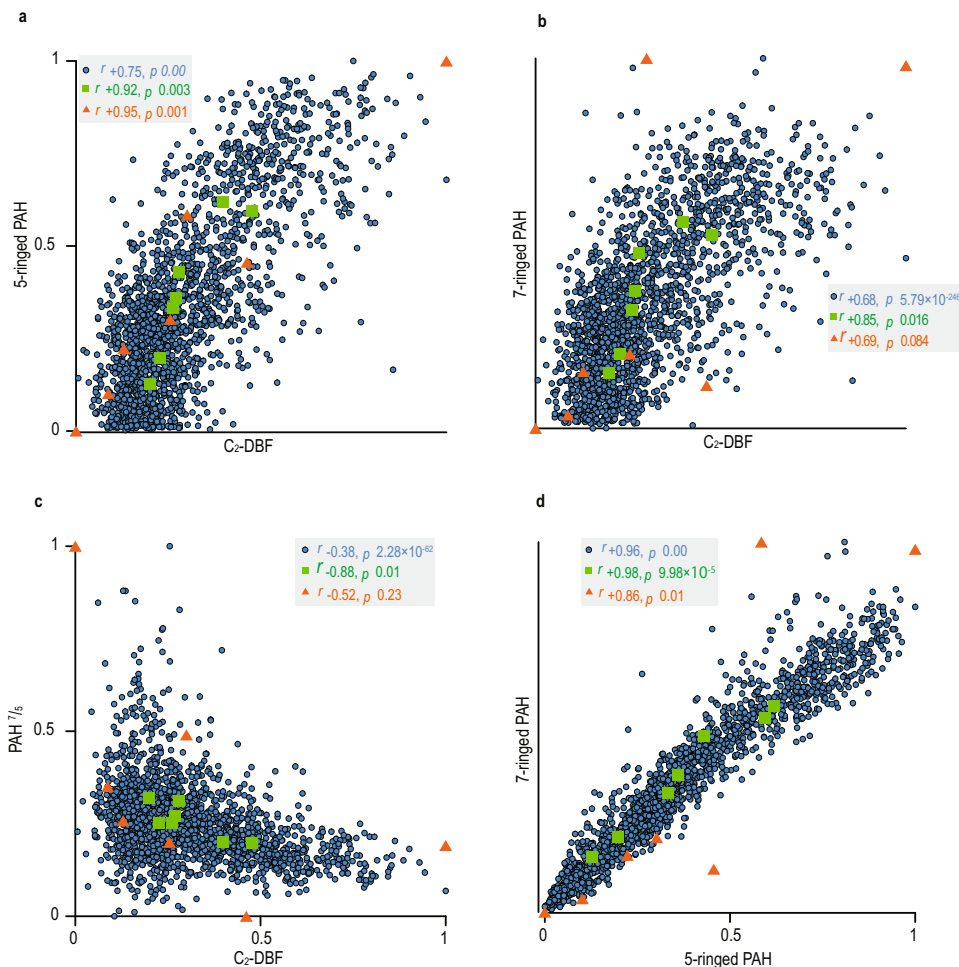


**Fig. 3 | Pyrogenic PAHs vs. soil organic matter.** Cross-plots of molecular biomarkers for pairs of five-ringed PAH and C<sub>2</sub>-DBF (a), seven-ringed PAH and C<sub>2</sub>-DBF (b), PAH<sup>7/5</sup> and C<sub>2</sub>-DBF (c), and seven- and five-ringed PAHs (d). The seven- and five-ringed PAHs and PAH<sup>7/5</sup> are shown as markers for combustion and combustion temperature, respectively (see text), and C<sub>2</sub>-DBF as markers for soil organic matter. Blue circles: MSI data; orange triangles: GC-MS data; green squares: the mean values of MSI data corresponding to the stratigraphic range for each sample of GC-MS

data. Pearson's  $r$  values ( $r$ ) and  $p$  values ( $p$ ) are shown in the plots. For MSI data, the sample size is 1863, 1821, 1776, and 1823 in plots a–d, respectively. For MSI mean and GC-MS data sample size is  $n = 7$  in all plots. MSI and GC-MS data are normalized to their maximum values. Because of the large sample size of the MSI data, its  $p$  value is prone to be smaller than  $<0.05$ , so the correlation coefficient and  $p$  value were also calculated for the mean value of MSI data. Note that as the contribution of C<sub>2</sub>-DBF increases, the PAH<sup>7/5</sup> ratio decreases.

identified as a turning point of terrestrial and marine ecosystem deterioration. Events 4 and 7 finally resulted in euxinia as indicated by the accumulation of framboidal pyrite, S, Fe, and pyrite laminae. Euxinia was probably caused by fertilization through terrestrial runoff that provided excess nutrients to the marine realm and reduced dissolved oxygen due to the aerobic decomposition of planktonic organic matter. Consequently, events 4 and 7 show highly characteristic maxima in wildfires and soil weathering, closely followed by maxima in bedrock weathering and/or soil leaching, and finally, euxinia. For event 8, for which maxima in PAH abundances and PAH<sup>7/5</sup> were recorded, Al, S, and Fe peaks are not observed, but are expected to be part of the subsequent ash bed (Bed 25-1) as pyrite laminae have been reported at the base of this bed<sup>42</sup>.

Our dataset records a temporal sequence of high-resolution environmental deterioration that is consistent with previous, less detailed observations and thus clearly extends the insights into the centennial to millennial-scale interplay of environmental stressors leading to the EPME. Wildfires can severely damage vegetation cover<sup>43</sup>, although ecosystems generally recover from these episodes relatively rapidly, i.e., within decades<sup>1</sup>. However, as the intensity and/or frequency of wildfires increased and was amplified by additional stressors derived from Siberian Traps volcanism (e.g., acid rain, changes in solar

radiation, aridity resulting from global warming)<sup>1,44</sup>, they seem to have contributed to the devastation of the terrestrial ecosystem<sup>33</sup>. At the end of the Permian, enhanced nutrient supply to the oceans from soil runoff<sup>47</sup> as a consequence of wildfires<sup>33</sup> would have been combined with global warming<sup>44</sup> and continental shelf weathering<sup>45</sup> related to exposure of vast continental shelves due to rapid marine regression<sup>46</sup>. These nutrients would have led to a substantial spike in marine primary productivity and oxygen consumption, ultimately resulting in euxinic water column conditions<sup>4,47,48</sup> that triggered the end-Permian mass extinction of marine metazoans. This sequence of volcanism-weathering-anoxia has also been suggested by a geochemical modeling study on much longer time scales<sup>49</sup>. However, we show that the interactions of environmental changes on land with those in the ocean took place at decadal to centennial time scales, and that irreversible tipping points were crossed as a consequence. Thus, the thermal evolution of the Earth's interior taking place on long geological time scales and expressed as the Siberian Traps episode, ultimately led to abrupt environmental changes at the Earth's surface.

#### Timing of terrestrial and marine crises

The timing of the marine and terrestrial crises at the end of the Permian is under debate. In high-latitude Australian terrestrial sections,



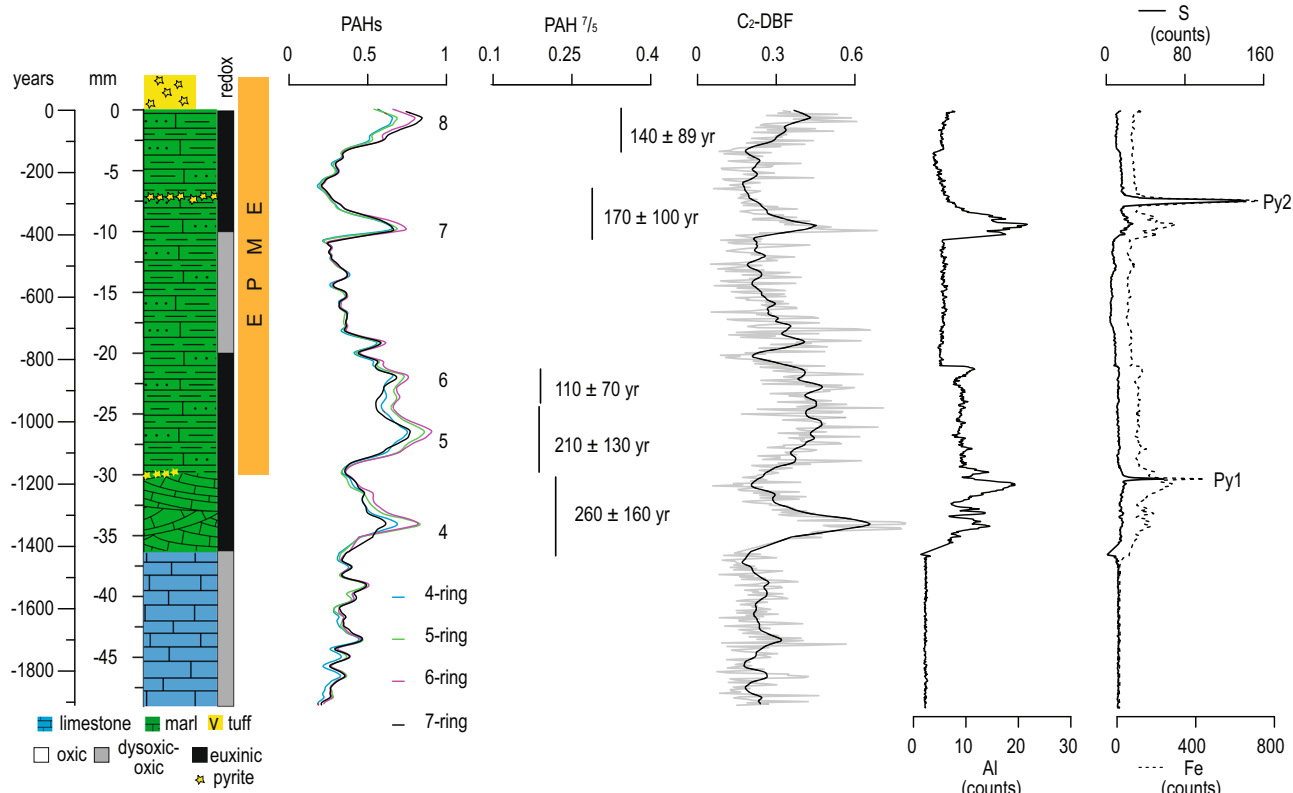


**Fig. 4 | A high-resolution record from the top of Bed 24e.** The four- to seven-ringed PAHs and mean values of PAH<sup>7/5</sup> for events 4–8 are shown as combustion markers and combustion temperature, respectively. C<sub>2</sub>-DBF and Al are shown as markers for soil and clastic input, respectively. S and Fe are shown to indicate the

existence of pyrite spikes. The numbers from 4 to 8 along the plot are denoted as episodes of increased PAH input. The redox bar is after the framboidal pyrite data of ref. 39. Py 1 and Py 2 are indicating pyrite spikes. EPME is after ref. 21. The relative age model is based on a mean-weighted sedimentation rate (2.6 cm/kyr)<sup>8</sup> (see text).

where the extinction is well studied on a multiple-basin scale, extinction occurred from  $252.54 \pm 0.08$  to  $252.10 \pm 0.06$  Ma<sup>50</sup>. However, the temporal relationship between the terrestrial and marine crises in Australia is unknown because the marine extinction cannot be well defined in the Australian predominantly continental sections. Meanwhile, numerous sections in South China (including the GSSP Meishan section) are set in a near-shore setting, thereby affording information from both the marine and terrestrial realms. At the low-latitude South China sections, the marine extinction, starting at  $251.941 \pm 0.037$  Ma<sup>8</sup>, was preceded by a terrestrial crisis<sup>51,52</sup>. Our high-resolution analysis confirms these previous findings<sup>51,52</sup> and further demonstrates how environmental stressors leading to extinctions on land and in the ocean are interrelated at the centennial to millennial scales. Namely, this study shows that the terrestrial crisis occurs ~300 yr (120–480 yr and  $\pm 2$  s.d.) prior to the onset of the marine extinction in South China. Thus, the terrestrial environmental degradation and extinction at high southern latitudes was 200–600 kyr earlier than at low latitudes. Factors that explain regional differences in the timing of extinction are unknown, but in addition to the Siberian Traps volcanism, attention is beginning to focus on the localized ecological impact of the extensive circum-Pangean felsic volcanism ‘Pangean ring of fire’ that encircled the amalgamated continents during the late Permian<sup>48,53,54</sup>. Further paleontological, geochemical, and chronological studies are needed to understand the regional interplay and timing of terrestrial and marine extinctions.

## Methods

### Samples

Sedimentary rock samples were taken from an outcrop of the uppermost Permian Changxing Fm. in the Meishan C section, Zhejiang Province of South China ( $31^{\circ}4'36.74''\text{N}$ ,  $119^{\circ}41'52.80''\text{E}$ ) (Fig. 1). The

depositional setting at the Meishan section was mid-slope<sup>27</sup>. Lithologically, the upper Permian, consisting of limestone with frequent lamination, is distinctive from the overlying Lower Triassic strata<sup>27</sup> of argillaceous, soft sedimentary rocks. A diamond saw with a beforehand baked blade was used to cut the rock into subsections with minimized contamination. The size of subsections was maintained at less than 5 (height)  $\times$  15 (width)  $\times$  50 (length) mm in order to fit into the custom-made MSI sample holders. Subsections were fixed in the MSI sample holders with double-sided conducting tape and stored in a desiccator until elemental mapping and measurement by MSI. In total, we investigated a section of 20 cm in length originating from Bed 24d to Bed 25. Following previous studies<sup>21,32</sup>, the top of Bed 24e is set to 0 years (or 0 m).

### Age model

The Meishan section is well-constrained by high-resolution U-Pb zircon dating<sup>8,55</sup>. A linear high-resolution age model was constructed using a weighted-mean sedimentation rate calculated in a Monte Carlo simulation in ref. 8. With this mean-weighted rate of 2.6 cm/kyr (minimum: 1.6 cm/kyr; maximum: 6.5 cm/kyr) in Beds 22 to 25 in the Meishan section<sup>8</sup>, the resolution of our analysis corresponds to 3.9 yr (minimum: 1.5 yr; maximum: 6.3 yr), and is therefore sufficient to reveal short-term, pulsed volcanism and related environmental disturbances.

However, we note that some uncertainty remains when assuming a linear sedimentation rate since major environmental and biotic changes are recorded by the lithological changes towards the top of Bed 24. While the decrease in carbonate-producing biota towards the top of Bed 24<sup>42</sup> would result in a decrease in sedimentation rate, this decrease in sedimentation rate was likely compensated by the simultaneously increased rate of soil influx and bedrock weathering<sup>56</sup>. The Bayesian Bchron age model for the Meishan section indicates that the

sedimentation rate became progressively higher towards the top of Bed 24<sup>57</sup>. This would imply an increasing temporal resolution toward the top of Bed 24.

### Ultra-high-resolution mass spectrometry imaging (MSI)

A 7 T solariX XR FT-ICR-MS equipped with a Smartbeam II laser (Bruker Daltonik, Bremen, Germany) was used for MSI. The laser scanned the sample in a defined area with a distance of 100  $\mu\text{m}$  between spots. Laser power, frequency, and the number of shots per spot were adjusted for optimal signal intensities.

PAHs and C<sub>2</sub>-DBF were identified based on their monoisotopic mass. External mass calibration was done using a NaTFA solution<sup>58</sup> in positive-ion mode with electrospray ionization in a mass-to-charge range of 150–750  $m/z$ , followed by an internal lock mass calibration using the  $m/z$  value 179.9995 (C<sub>15</sub>) in DataAnalysis 4.4 SRI (Bruker Daltonik). Clusters composed solely of carbon atoms up to C<sub>60</sub> were detected in abundance in our samples. After calibration,  $m/z$ , intensity, and signal-to-noise ratio of the targeted PAH and C<sub>2</sub>-DBF species were exported together with their xy-coordinates for further processing in MATLAB R2015b using a DataAnalysis Script File. To avoid storing low-intensity noise signals and assure high data quality, all MSI data were acquired with 25% data reduction. Additionally, a signal-to-noise ratio of 3 was applied as a filter. Analogous procedures for ensuring high-quality signals have been successfully used in previous studies of MSI<sup>59,60</sup>. Lowess smoothing of MSI data was conducted using Origin (2018) software with a span value = 0.01.

### Elemental mapping

Elemental mapping was performed on an M4 Tornado Micro-XRF spectrometer system (Bruker Nano Analytics) equipped with a micro-focused Rh source (50 kV and 600  $\mu\text{A}$ ) with poly-capillary optics (25- $\mu\text{m}$  spot size). Measurements were conducted under vacuum (20 mb) conditions with a resolution of 50  $\mu\text{m}$  per pixel and a scan time of 60 ms per pixel. Map data were initially processed and visualized with M4 Tornado Software version 1.3. Distribution maps of Al, Fe, and S (counts) were exported as xy-matrices to csv files and further processed.

### Conventional GC-MS analysis

Seven sediment samples (0 to –1 cm, –1 to –2 cm, –2 to –4 cm, –4 to –8 cm, –8 to –13 cm, –13 to –16 cm, and –16 to –20 cm) were ground with an agate mortar. The ~3 g of powdered samples were then ultrasonically extracted five times with toluene:MeOH (9:1). The extracts were transferred into 60 ml vials and carefully concentrated under a stream of N<sub>2</sub>. The concentrated extracts were separated into non-polar and polar fractions using silica gel chromatography. The non-polar fraction and polar fraction were obtained by elution with *n*-hexane:DCM (4:1) and DCM:MeOH (4:1), respectively. The non-polar fraction was analyzed by GC-MS on an Agilent gas chromatograph (GC, 6890) interfaced with an Agilent 5975 mass selective detection (MSD) instrument. A DB-5MS column (60 m  $\times$  250  $\mu\text{m}$   $\times$  0.25  $\mu\text{m}$ ) was installed with the GC oven. We used a temperature program of: isothermally at 40 °C for 2 min, ramped to 320 °C at a rate of 4°/min, and then held at this temperature for 22 min. PAHs (four-ringed PAH: pyrene and fluoranthene; five-ringed PAH: benzo[e]pyrene, benzo[a]pyrene, and benzo[b]/j/k]fluoranthene; 6-ringed PAH: indeno[1,2,3-cd]pyrene and benzo[ghi]perylene; seven-ringed PAH: coronene) and C<sub>2</sub>-DBF were identified (Supplementary Fig. 4) based on a comparison of mass spectra and relative GC scan numbers with published data<sup>61,62</sup>.

### Data analysis

In order to assess the strength of periodicities of combustion events at different times and for different periods, wavelet analysis using the Morlet wavelet was performed on PAH data using the Paleontological Statics (PAST) software package developed by ref. 63. The Pearson's

correlation test was used to explore collinearity between biomarkers and  $p$  values were calculated to evaluate statistical significance.

### Data availability

All data generated in this study have been deposited in the PANGAEA data repository under access code <https://doi.org/10.1594/PANGAEA.952297>.

### Code availability

The latest version of the PAST software package is available at <https://www.nhm.uio.no/english/research/resources/past/> along with the User's manual to generate the results for the paper. The code in the Past is based on Torrence and Compo<sup>64</sup>.

### References

1. Benton, M. J. Hyperthermal-driven mass extinctions: killing models during the Permian-Triassic mass extinction. *Philos. Trans. R. Soc. A Math. Phys. Eng. Sci.* **376**, 1–19 (2018).
2. Svensen, H. et al. Siberian gas venting and the end-Permian environmental crisis. *Earth Planet. Sci. Lett.* **277**, 490–500 (2009).
3. Burgess, S. D., Muirhead, J. D. & Bowring, S. A. Initial pulse of Siberian traps sills as the trigger of the end-Permian mass extinction. *Nat. Commun.* **8**, 1–6 (2017).
4. Grice, K. et al. Photic zone euxinia during the Permian-triassic superanoxic event. *Science* **307**, 706–709 (2005).
5. Joachimski, M. M. et al. Climate warming in the latest Permian and the Permian-Triassic mass extinction. *Geology* **40**, 195–198 (2012).
6. Sanei, H., Grasby, S. E. & Beauchamp, B. Latest Permian mercury anomalies. *Geology* **40**, 63–66 (2012).
7. Burgess, S. D. & Bowring, S. A. High-precision geochronology confirms voluminous magmatism before, during, and after Earth's most severe extinction. *Sci. Adv.* **1**, 1–14 (2015).
8. Burgess, S. D., Bowring, S. & Shen, S. Z. High-precision timeline for Earth's most severe extinction. *Proc. Natl Acad. Sci. USA* **111**, 3316–3321 (2014).
9. Song, H., Wignall, P. B., Tong, J. & Yin, H. Two pulses of extinction during the Permian-Triassic crisis. *Nat. Geosci.* **6**, 52–56 (2013).
10. Pavlov, V. E., Fluteau, F., Veselovskiy, R. V., Fetisova, A. M. & Latshev, A. V. Secular geomagnetic variations and volcanic pulses in the Permian-Triassic traps of the Norilsk and Maimecha-Kotui provinces. *Izvestiya, Phys. Solid Earth* **47**, 402–417 (2011).
11. Black, B. A. et al. Systemic swings in end-Permian climate from Siberian Traps carbon and sulfur outgassing. *Nat. Geosci.* **11**, 949–954 (2018).
12. Grasby, S. E. et al. Isotopic signatures of mercury contamination in latest Permian oceans. *Geology* **45**, 55–58 (2017).
13. Wang, X. et al. Mercury anomalies across the end Permian mass extinction in South China from shallow and deep water depositional environments. *Earth Planet. Sci. Lett.* **496**, 159–167 (2018).
14. Shen, J. et al. Mercury fluxes record regional volcanism in the South China craton prior to the end-Permian mass extinction. *Geology* **49**, 452–456 (2020).
15. Shen, J. et al. Mercury evidence from southern Pangea terrestrial sections for end-Permian global volcanic effects. *Nat. Commun.* <https://doi.org/10.1038/s41467-022-35272-8> (2023).
16. Liu, Z., Selby, D., Zhang, H. & Shen, S. Evidence for volcanism and weathering during the Permian-Triassic mass extinction from Meishan (South China) osmium isotope record. *Palaeogeogr. Palaeoclimatol. Palaeoecol.* **553**, 1–6 (2020).
17. Sephton, M. A. et al. Catastrophic soil erosion during the end-Permian biotic crisis. *Geology* **33**, 941–944 (2005).
18. Dal Corso, J. et al. Permo-Triassic boundary carbon and mercury cycling linked to terrestrial ecosystem collapse. *Nat. Commun.* **11**, 1–9 (2020).

19. Fielding, C. R. et al. Age and pattern of the southern high-latitude continental end-Permian extinction constrained by multiproxy analysis. *Nat. Commun.* **10**, 1–12 (2019).
20. Van De Schootbrugge, B. et al. Floral changes across the Triassic/Jurassic boundary linked to flood basalt volcanism. *Nat. Geosci.* **2**, 589–594 (2009).
21. Kaiho, K., Aftabuzzaman, M., Jones, D. S. & Tian, L. Pulsed volcanic combustion events coincident with the end-Permian terrestrial disturbance and the following global crisis. *Geology* **49**, 289–293 (2021).
22. Arinobu, T., Ishiwatari, R., Kaiho, K. & Lamolda, M. A. Spike of pyrosynthetic polycyclic aromatic hydrocarbons associated with an abrupt decrease in  $\delta^{13}\text{C}$  of a terrestrial biomarker at the Cretaceous-Tertiary boundary at Caravaca, Spain. *Geol. Soc. Am. Bull.* **27**, 723–726 (1999).
23. Pastorova, I., Botto, R. E., Arisz, P. W. & Boon, J. J. Cellulose char structure: a combined analytical Py-GC-MS, FTIR, and NMR study. *Carbohydr. Res.* **262**, 27–47 (1994).
24. Shen, W., Sun, Y., Lin, Y., Liu, D. & Chai, P. Evidence for wildfire in the Meishan section and implications for Permian–Triassic events. *Geochim. Cosmochim. Acta* **75**, 1992–2006 (2011).
25. Wörmer, L. et al. Ultra-high-resolution paleoenvironmental records via direct laser-based analysis of lipid biomarkers in sediment core samples. *Proc. Natl Acad. Sci. USA* **111**, 15669–15674 (2014).
26. Wörmer, L. et al. Towards multiproxy, ultra-high resolution molecular stratigraphy: Enabling laser-induced mass spectrometry imaging of diverse molecular biomarkers in sediments. *Org. Geochem.* **127**, 136–145 (2019).
27. Yin, H., Zhang, K., Tong, J., Yang, Z. & Wu, S. The global stratotype section and point (GSSP) of the Permian-Triassic Boundary. *Epiisodes* **24**, 102–114 (2001).
28. Jin, Y. et al. The global boundary stratotype section and point (GSSP) for the base of Changhsingian stage (Upper Permian). *Epiisodes* **29**, 175–182 (2006).
29. Yuan, D.-x et al. Revised conodont-based integrated high-resolution timescale for the Changhsingian Stage and end-Permian extinction interval at the Meishan sections, South China. *Lithos* **204**, 220–245 (2014).
30. Lyons, T. W. & Severmann, S. A critical look at iron paleoredox proxies: new insights from modern euxinic marine basins. *Geochim. Cosmochim. Acta* **70**, 5698–5722 (2006).
31. Sheldon, N. D. & Tabor, N. J. Quantitative paleoenvironmental and paleoclimatic reconstruction using paleosols. *Earth Sci. Rev.* **95**, 1–52 (2009).
32. Kaiho, K., Chen, Z.-Q., Kawahata, H., Kajiwara, Y. & Sato, H. Close-up of the end-Permian mass extinction horizon recorded in the Meishan section, South China: sedimentary, elemental, and biotic characterization and a negative shift of sulfate sulfur isotope ratio. *Palaeogeogr. Palaeoclimatol. Palaeoecol.* **239**, 396–405 (2006).
33. Mays, C. & McLoughlin, S. End-Permian burnout: the role of Permian-Triassic wildfires in extinction, carbon cycling and environmental change in eastern Gondwana. *PALAIOS* **37**, 292–317 (2022).
34. Cronan, C. S. & Schofield, C. L. Aluminum leaching response to acid precipitation: effects on high-elevation watersheds in the Northeast. *Science* **204**, 304–306 (1979).
35. Norinaga, K., Deutschmann, O., Saegusa, N. & Hayashi, J. Analysis of pyrolysis products from light hydrocarbons and kinetic modeling for growth of polycyclic aromatic hydrocarbons with detailed chemistry. *J. Anal. Appl. Pyrolysis* **86**, 148–160 (2009).
36. Makkonen, U., Hellén, H., Anttila, P. & Ferm, M. Size distribution and chemical composition of airborne particles in south-eastern Finland during different seasons and wildfire episodes in 2006. *Sci. Total Environ.* **408**, 644–651 (2010).
37. Wang, Y. et al. Quantifying the process and abruptness of the end-Permian mass extinction. *Paleobiology* **40**, 113–129 (2014).
38. Shen, S.-Z. et al. A sudden end-Permian mass extinction in South China. *Geol. Soc. Am. Bull.* **131**, 205–223 (2018).
39. Wei, H., Zhang, X. & Qiu, Z. Millennial-scale ocean redox and  $\delta^{13}\text{C}$  changes across the Permian–Triassic transition at Meishan and implications for the biocrisis. *Int. J. Earth Sci.* **109**, 1753–1766 (2020).
40. Roberts, W. M. B., Walker, A. L. & Buchanan, S. The chemistry of pyrite formation in aqueous solution and its relation to the depositional environment. *Minera. Depos.* **4**, 18–29 (1969).
41. French, K. L., Tosca, N. J., Cao, C. Q. & Summons, R. E. Diagenetic and detrital origin of moretane anomalies through the Permian-Triassic boundary. *Geochim. Cosmochim. Acta* **84**, 104–125 (2012).
42. Chen, Z.-Q. et al. Complete biotic and sedimentary records of the Permian–Triassic transition from Meishan section, South China: ecologically assessing mass extinction and its aftermath. *Earth Sci. Rev.* **149**, 67–107 (2015).
43. Kump, L. R. Terrestrial feedback in atmospheric oxygen regulation by fire and phosphorus. *Nature* **335**, 152–154 (1988).
44. Wang, W.-Q. et al. A high-resolution Middle to Late Permian paleotemperature curve reconstructed using oxygen isotopes of well-preserved brachiopod shells. *Earth Planet. Sci. Lett.* **540**, 1–14 (2020).
45. Wang, J. et al. Coupled  $\delta^{44}\text{Ca}$ / $^{40}\text{Ca}$ ,  $\delta^{88}\text{Sr}$ / $^{86}\text{Sr}$ , and  $^{87}\text{Sr}$ / $^{86}\text{Sr}$  geochemistry across the end-Permian mass extinction event. *Geochim. Cosmochim. Acta* **262**, 143–165 (2019).
46. Yin, H. F. et al. The end-Permian regression in South China and its implication on mass extinction. *Earth Sci. Rev.* **137**, 19–33 (2014).
47. Xiang, L. et al. Oceanic redox evolution around the end-Permian mass extinction at Meishan, South China. *Palaeogeogr. Palaeoclimatol. Palaeoecol.* **544**, 1–12 (2020).
48. Vajda, V. et al. End-Permian (252 Mya) deforestation, wildfires and flooding—An ancient biotic crisis with lessons for the present. *Earth Planet. Sci. Lett.* **529**, 1–12 (2020).
49. Jurikova, H. et al. Permian-Triassic mass extinction pulses driven by major marine carbon cycle perturbations. *Nat. Geosci.* **13**, 1–6 (2020).
50. Fielding, C. R. et al. Sedimentology of the continental end-Permian extinction event in the Sydney Basin, eastern Australia. *Sedimentology* **68**, 30–62 (2021).
51. Aftabuzzaman, M. et al. End-Permian terrestrial disturbance followed by the complete plant devastation, and the vegetation proto-recovery in the earliest-Triassic recorded in coastal sea sediments. *Glob. Planet. Change* **205**, 1–19 (2021).
52. Chu, D. et al. Ecological disturbance in tropical peatlands prior to marine Permian-Triassic mass extinction. *Geology* **48**, 288–292 (2020).
53. Zhang, H. et al. Felsic volcanism as a factor driving the end-Permian mass extinction. *Sci. Adv.* **7**, 1–13 (2021).
54. Chapman, T., Milan, L. A., Metcalfe, I., Blevin, P. L. & Crowley, J. Pulses in silicic arc magmatism initiate end-Permian climate instability and extinction. *Nat. Geosci.* **15**, 411–416 (2022).
55. Shen, S. Z. et al. Calibrating the end-Permian mass extinction. *Science* **334**, 1367–1372 (2011).
56. Algeo, T. J. & Twitchett, R. J. Anomalous Early Triassic sediment fluxes due to elevated weathering rates and their biological consequences. *Geology* **38**, 1023–1026 (2010).
57. Baresel, B. et al. Precise age for the Permian–Triassic boundary in South China from high-precision U-Pb geochronology and Bayesian age–depth modeling. *Solid Earth* **8**, 361–378 (2017).
58. Moini, M., Jones, B. L., Rogers, R. M. & Jiang, L. Sodium trifluoroacetate as a tune/calibration compound for positive- and negative-ion electrospray ionization mass spectrometry in the mass range of 100–4000 Da. *J. Am. Soc. Mass Spectrom.* **9**, 977–980 (1998).

59. Wörmer, L. et al. A micrometer-scale snapshot on phototroph spatial distributions: mass spectrometry imaging of microbial mats in Octopus Spring, Yellowstone National Park. *Geobiology* **18**, 742–759 (2020).
60. Obreht, I. et al. Last Interglacial decadal sea surface temperature variability in the eastern Mediterranean. *Nat. Geosci.* **15**, 812–818 (2022).
61. Mita, H. GC/MS analysis of polycyclic aromatic hydrocarbons in the Cretaceous-Tertiary boundary sediments. *Res. Org. Geochem.* **20**, 49–64 (2005).
62. Watson, J. S., Sephton, M. A., Looy, C. V. & Gilmour, I. Oxygen-containing aromatic compounds in a Late Permian sediment. *Org. Geochem.* **36**, 371–384 (2005).
63. Hammer, Ø., Harper, D. A. T. & Ryan, P. D. PAST-palaeontological statistics, ver. 1.89. *Palaeontol. Electron.* **4**, 1–9 (2001).
64. Torrence, C. & Compo, G. P. A practical guide to wavelet analysis. *Bull. Am. Meteorol. Soc.* **79**, 61–78 (1998).

## Acknowledgements

This study was financed by Overseas Research Fellowships (to R.S.) of the Ministry of Education, Culture, Sports, Science, and Technology, Japan. R.S. also acknowledges support from JST PRESTO (grant number JPMJPR19G5; Japan). This study was supported by the Japan Society for the Promotion of Science (grant no. 25247084) (to K.K.) and the National nature science foundation of China (grant no. 42030513) (to L.T.). Research at the University of Bremen was supported by the European Research Council under the European Union's Horizon 2020 Research and Innovation Program, grant agreement No. 670115 ZOOMECULAR (K.-U.H.); research at Massachusetts Institute of Technology was supported by the Simons Foundation Collaboration on the Origins of Life (290361FY18 to R.E.S.). The  $\mu$ -XRF system was financed by the Deutsche Forschungsgemeinschaft with funds granted to the University of Bremen in the framework of the Excellence Initiative. We thank Masahiro Oba and Haijun Song for their help with sampling in the field. We also thank Dr. Christian Hallmann for his support with sample preparation at Bremen University.

## Author contributions

R.S. and K.-U.H. planned this study. K.-U.H. and R.E.S. provided analytical infrastructure and protocols. K.K. and S.T. sampled rocks. M.I. and R.S. conducted wavelet analyses. L.W. and R.S. conducted MSI analyses. R.S. conducted GC-MS analyses. H.T. and R.S. conducted micro-XRF

analyses. R.S. and L.W. wrote the paper with insight provided by H.T., L.T., S.T., K.K., M.I., K.-U.H., and R.E.S. R.E.S. edited the paper.

## Funding

Open Access funding enabled and organized by Projekt DEAL.

## Competing interests

The authors declare no competing interests.

## Additional information

**Supplementary information** The online version contains supplementary material available at <https://doi.org/10.1038/s41467-023-37717-0>.

**Correspondence** and requests for materials should be addressed to Ryosuke Saito.

**Peer review information** *Nature Communications* thanks Chris Mays, Vivi Vajda and the other, anonymous, reviewer(s) for their contribution to the peer review of this work.

**Reprints and permissions information** is available at <http://www.nature.com/reprints>

**Publisher's note** Springer Nature remains neutral with regard to jurisdictional claims in published maps and institutional affiliations.

**Open Access** This article is licensed under a Creative Commons Attribution 4.0 International License, which permits use, sharing, adaptation, distribution and reproduction in any medium or format, as long as you give appropriate credit to the original author(s) and the source, provide a link to the Creative Commons license, and indicate if changes were made. The images or other third party material in this article are included in the article's Creative Commons license, unless indicated otherwise in a credit line to the material. If material is not included in the article's Creative Commons license and your intended use is not permitted by statutory regulation or exceeds the permitted use, you will need to obtain permission directly from the copyright holder. To view a copy of this license, visit <http://creativecommons.org/licenses/by/4.0/>.

© The Author(s) 2023